Noninjection Gram-Scale Synthesis of Monodisperse Pyramidal $CuInS_2$ Nanocrystals and Their Size-Dependent Properties

Haizheng Zhong,[†,⊥] Shun S. Lo,[†] Tihana Mirkovic,[†] Yunchao Li,[‡] Yuqin Ding,[§] Yongfang Li,[§] and Gregory D. Scholes[†,*]

[†]Department of Chemistry, 80 St. George Street, Institute for Optical Sciences, and Center for Quantum Information and Quantum Control, University of Toronto, Toronto, Ontario, M5S 3H6 Canada, [‡]Department of Chemistry, Beijing Normal University, Beijing, 100875, China, and [§]Beijing National Laboratory for Molecular Sciences, Institute of Chemistry, Chinese Academy of Sciences, Beijing 100190, China. [⊥]Current Address: School of Materials Science and Engineering, Beijing Institute of Technology, Beijing 100081, China.

ABSTRACT $CuInS_2$ nanocrystals are viewed as very good candidates for solar harvesting and light emitting applications. Here we report an optimized noninjection method for the synthesis of monodisperse pyramidal $CuInS_2$ nanocrystals with sizes ranging from 3 to 8 nm. This synthetic route is able to yield large amounts of high quality nanoparticles, usually in the gram scale for one batch experiment. The structure and surface studies showed that the resulting nanocrystals are pyramids of $CuInS_2$ tetragonal phase with well-defined facets, while their surface is functionalized with dodecanethiol capping ligands. Spectroscopic and electrochemical measurements revealed size-dependent optical and electrical properties of $CuInS_2$ nanocrystals, demonstrating quantum confinement effects in these systems. The size-dependent optical bandgaps of $CuInS_2$ nanocrystals were found to be consistent with the finite-depth well effective mass approximation (EMA) calculations, which provide a convenient method to estimate the diameter of $CuInS_2$ pyramids. Additionally we have also determined some important physical parameters, including bandgaps and energy levels, for this system, which are crucial for the integration of $CuInS_2$ nanocrystals in potential device applications.

KEYWORDS: noninjection method · $CuInS_2$ nanocrystals · light emitters · solar harvesters · quantum confinement effects · energy levels · cyclic voltammetry

Colloidal semiconductor nanocrystals (NCs) have shown great potential in applications as light-emitting and solar-harvesting materials since their optical properties can be tuned by size and shape due to quantum-confinement effects.[1−3] For device applications, it is crucial that the nanocrystalline materials are of high quality, exhibiting narrow size and shape distributions, with a good colloidal stability, and a high crystallinity. To date numerous synthetic methodologies have been developed for the production of high quality cadmium- or lead-based NCs for biolabeling,[4] lasers,[5] light-emitting diodes,[6] and solar cell applications.[7−9] However, cadmium- or lead-based NCs have a doubtful future because of their high toxicity, and more recently researchers have turned their attention to ternary nontoxic I−III−VI compounds such as $CuInS_2$ and $CuInSe_2$ NCs.[10−15]

Bulk $CuInS_2$ has a direct bandgap of 1.53 eV, which is well matched with the optimal spectral range for photovoltaic applications, resulting in $CuInS_2$ NCs having great potential as solar harvesters for a new generation of solution processed solar cells.[16−20] Recent reports have demonstrated the potential of using $CuInS_2$ NCs in solar cell devices with power conversion efficiencies approaching ~5%.[17−19] In addition, $CuInS_2$ NCs exhibit size tunable emission in the red to near-infrared (NIR) region (550−850 nm) for the NCs with diameters comparable to the exciton Bohr radius (~4.1 nm for $CuInS_2$). Furthermore, nanomaterials with light emission in this wavelength region are of importance in biolabeling and light-emitting diodes.[2,4]

It is highly desirable that synthetic methods which are aimed at producing high quality nanomaterials for potential industrial applications are scalable, reproducible, environmentally friendly, and low cost, while enabling the production of nanocrystals in a high yield. Several synthetic methodologies for the production of $CuInS_2$ NCs at the multigram-scale have been explored, including the hot-injection method,[15,21−25] hydrothermal techniques,[26,27] chemical transformation route,[28] and thermal decomposition of suitable precursors.[29−34] Since size, morphology, elemental stoichiometry, and crystal symmetry are known to

*Address correspondence to gscholes@chem.utoronto.ca.

Received for review July 7, 2010 and accepted August 30, 2010.

Published online September 3, 2010. 10.1021/nn1015538

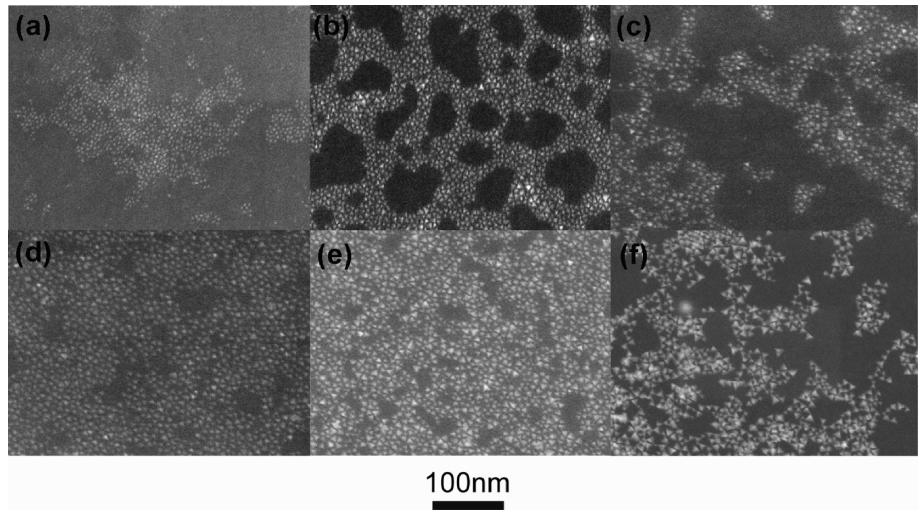

Figure 1. STEM images of $CuInS_2$ NCs with diameters of (a) 3.5 ± 0.4, (b) 4.6 ± 0.6, (c) 5.2 ± 0.7, (d) 5.6 ± 0.7, (e) 6.1 ± 1.1, and (f) 7.3 ± 1.4 nm. These samples were prepared under identical synthetic conditions with varying reaction times of 20, 30, 45, 60, 90, and 120 min, respectively.

influence the properties of $CuInS_2$ NCs, it is of great interest to further explore the synthetic routes to achieve control and tunability of these vital parameters.

We recently developed a noninjection thermal decomposition route for the synthesis of $CuInS_2$ NCs with tunable absorption and emission spectra by heating inorganic metal salt and an alkanethiol complex.[35] A similar method has also been successfully employed by Li *et al.* in the synthesis of luminescent $CuInS_2$/ZnS NCs.[36] However, the resulting $CuInS_2$ NCs exhibited poor crystallinity and a large size distribution. In the current work, this synthetic method is further refined to give high quality monodisperse $CuInS_2$ NCs in a high yield. The as prepared $CuInS_2$ NCs have a pyramidal morphology and their diameters (determined by measuring the average edge lengths of pyramids, for a schematic diagram see Supporting Information Figure S1) can be easily tuned between ~3 and 8 nm by adjusting the reaction time. The chemical and physical characteristics of $CuInS_2$ NCs were investigated, including their size-dependent optical and electronic properties, which present some crucial parameters for the integration of these high quality materials in light emitting and solar harvesting applications.

RESULTS AND DISCUSSIONS

Synthetic Strategy. It has been known that the key to synthesizing monodisperse ternary NCs is to balance the reactivity of the two cationic precursors by their ligands, solvent matrix composition, and reaction temperature. Our previous work employed three components: indium acetate, copper acetate, and dodecanethiol.[35] CuAc, $In(Ac)_3$, and dodecanethiol initially react to form an intermediate complex. Upon heating, the complex acts as the precursor and decomposes into $CuInS_2$ particles, as the reaction time progresses. When the size of formed $CuInS_2$ nanoparticles exceeds 3 nm, the nanoparticles are likely to aggregate and precipitate from the solution upon continuous heating. This could be attributed to the fast reaction between metal ions with dodecanethiol, which consumes the monomers quickly and results in the aggregation process. Taking that into consideration, the reaction system was modified as to decrease the reaction rate. (1) We use CuI to substitute for CuAc. According to the "hard−soft acid−base model", Cu^+ is a soft acid and Ac^- is a hard base, whereas iodide and thiols (R-SH) are soft bases, where $I^- >$ HSR when the softness character is compared. Soft acid and soft base bind more tightly than soft base and hard acid pairs.[37] Therefore, the binding between I^- with Cu^+ is stronger than R-SH, slowing down the reactions between Cu^+ and the S source (R-SH). (2) We also introduce oleic acid to decrease the reaction between indium ions with R-SH. (3) The reaction temperature was decreased to slow down the reactions.

In our previous synthesis, we have observed that the reaction system can produce some $CuInS_2$ NCs with nonspherical shapes by adding oleic acid.[35] Here, we also considered the synthetic chemistry to improve the uniformity of $CuInS_2$ NCs with nonspherical shapes. Inherently, nonspherical particles such as cubes and tetrahedral pyramids have a higher surface energy than spherical particles and require growth conditions characterized by a higher chemical potential.[38] In this $CuInS_2$ system, the higher chemical potential was achieved by increasing the concentration of reaction precursors.

Synthesis and Characterizations of $CuInS_2$ Pyramids. The reactions were systematically optimized, resulting in the successful synthesis of monodisperse $CuInS_2$ pyramids. The detail of material preparation can be seen in the Experimental Section. Figure 1 shows scanning transmission electron microscopy (STEM) images of NCs obtained after various reaction times ranging from 20 to

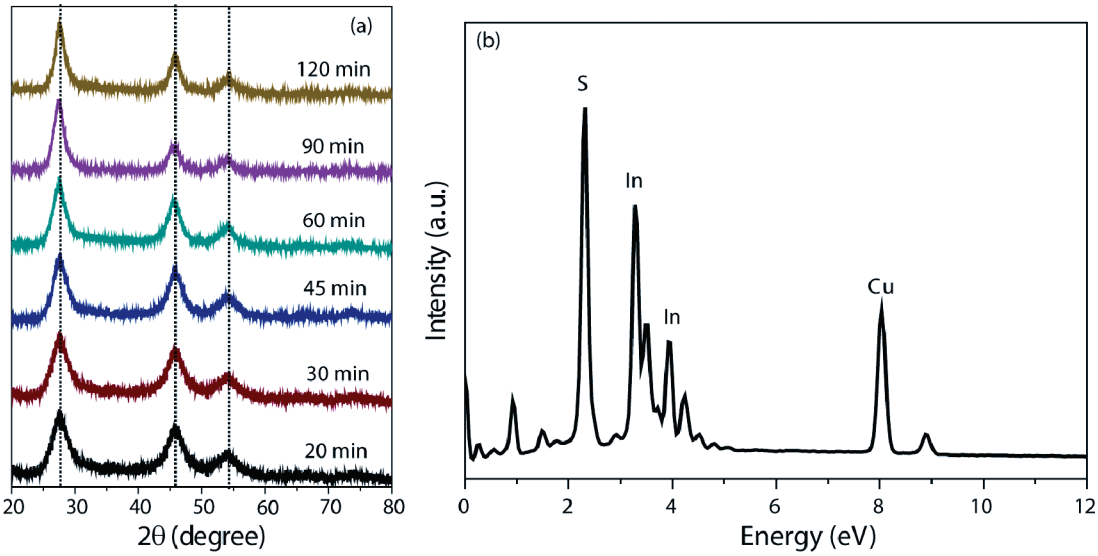

Figure 2. (a) XRD patterns of $CuInS_2$ NCs synthesized at different reaction times of 20, 30, 45, 60, 90, and 120 min. (b) A typical EDX spectrum of $CuInS_2$ NCs.

120 min. It was found that the resulting NCs exhibit pyramidal shapes. Their pyramidal shapes were further revealed in high magnification STEM images (see Supporting Information Figure S2). We determine their average diameters by measuring the average edge length of these pyramids. Detailed analysis indicates that these as-prepared NCs are nearly monodisperse, exhibiting diameters of 3.5 ± 0.4, 4.6 ± 0.6, 5.2 ± 0.7, 5.6 ± 0.7, 6.1 ± 1.1, and 7.3 ± 1.4 nm for the samples synthesized at reaction times of 20, 30, 45, 60, 90, and 120 min, respectively. Compared to our previous report (2 to ~5 nm),[35] the size tunability of $CuInS_2$ NCs are greatly extended.

The structural phases of the NCs were determined through X-ray diffraction (XRD) characterizations. Figure 2 shows the XRD patterns of the $CuInS_2$ NCs obtained at different reaction times. Although the difference between chalcopyrite phase and zincblende phases is very small, the $CuInS_2$ NCs with zincblende phase usually have a diffraction peak of (200).[23,31] In our work, the absent of this peak in the XRD patterns of $CuInS_2$ NCs can be an indirect evidence for the chalcopyrite phase. In addition, subsequent HRTEM results implied a chalcopyrite phase. Therefore, the XRD patterns were tentatively identified to reported chalcopyrite phase.[35] The first three diffraction peaks can be indexed to the (112), (204)/(220), and (116)/(312) reflections of the tetragonal crystal structure. In addition, XRD characterizations can also be used to determine the size evolution of NCs as a function of time by applying the Scherrer equation:

$$D_{\text{eff}} = K\lambda/B\cos(\theta_B) \quad (1)$$

where D_{eff} is the effective diameter determined by XRD, K is the Scherrer constant related to the shape of crystallites. λ is the X-ray wavelength, B is the full width at half-maximum of the diffraction peak, and θ_B is the half angle of the diffraction peak on the 2θ scale. Since the (112) plane of tetragonal phase equals to the (111) plane in cubic phase, we choose the Scherrer constant of 0.89 for tetrahedral crystallites perpendicular to the (111) plane in this caculation.[39]

The utility of the Scherrer equation for determination of the nanocrystal size in monodisperse systems has been demonstrated in detail in previous reports.[40−42] Since the broadening of Bragg reflections is determined by the number of unit cells along columns perpendicular to the diffraction planes, calculation of the particle size with the Scherrer equation usually leads to an effective diameter, D_{eff} which is usually smaller than the geometric diameter (d) (see Supporting Information Figure S3). Here we use $d = {}^3/_2 D_{\text{eff}}$, to estimate the mean geometric diameter (d_{XRD}) of $CuInS_2$ NCs from the (112) peaks (shown in Table 1), and we find these values to be in very good agreement with the results from STEM analysis. This shows that the properly adapted Scherrer equation is suitable for the determination of the size of the resulting pyramidal $CuInS_2$ NCs.

To obtain information about the chemical composition, energy dispersive X-ray (EDX) spectra and inductively coupled plasma atomic emission (ICP-AES) measurements were performed. A typical EDX spectrum is shown in Figure 2b, which confirmed the existence of Cu, In, and S elements in the as synthesized NCs. The elemental compositions of as prepared NCs were also determined by EDX and ICP−AES measurements (see Table 1). Temporal evolution of EDX measurements revealed that the evolving NCs are copper-rich (Cu:In composition of 1.71:1) in the early stage of the reaction. Then there is a continuous decrease of Cu with reaction time, resulting in a more stoichiometric composition (Cu:In composition of 1.03:1 and 0.94:1 for the resulting NCs obtained at 90 and 120 min, respectively)

TABLE 1. The Average Diameters and Elements Compositions of As-Prepared $CuInS_2$ NCs Determined by Corresponding Measurements

samples	S1 (20 min)	S2 (30 min)	S3 (45 min)	S4 (60 min)	S5 (90 min)	S6 (120 min)
$\langle d_{XRD} \rangle$ (nm)	3.6	4.0	5.1	5.5	6.1	7.6
$\langle d_{STEM} \rangle$ (nm)	3.5	4.6	5.2	5.6	6.1	7.3
Cu/In/S from EDX	1.71:1:2.1	1.56:1:2.2	1.36:1:1.8	1.21:1:1.83	1.03:1:1.9	0.92:1:1.91
Cu/In from ICP−AES	2.4:1	2.0:1	1.8:1	1.8:1	1.71:1	1.15:1

in the final stage. These results demonstrate that the Cu/In ratio in resulting $CuInS_2$ NCs shows a size-dependence. It is possible that the higher binding ability and reactivity of copper with dodecanethiol comparable to indium results in Cu-rich NCs during the initial growth stage, which is later recovered by reactivity of excess indium.

We further revealed the crystalline nature of the NCs by using high-resolution transmission electron microscopy (HRTEM) experiments (see Figure 3). The crystal quality was evidenced by the continuous lattice fringes and very clear crystal facets. On the basis of the HRTEM analysis, the observed lattice fringes with a distance of 0.320 nm can be identified to the (111) plane of the zincblende phase or the (112) plane of the chalcopyrite phase. If the $CuInS_2$ pyramids are of zincblende phase, then the four facets should be (111) face,[43,44] which is not consistent with the observation of the lattice fringes with a distance of 0.320 nm. Therefore, the $CuInS_2$ pyramids are of the chalcopyrite phase and the lattice fringes with a distance of 0.320 and 0.195 nm correspond to the (112) and (220) planes of the $CuInS_2$ chalcopyrite phase.[15] These results are similar to the observations in $CuInSe_2$ pyramids by Korgel *et al.*[45] The formation of pyramidal shapes can also be explained by using the "surface-facet polarity models". The $CuInS_2$ chalcopyrite structure is derived from the II−VI zincblende structure by substituting group I and group III Cu and In atoms for the group II atoms. The (112) plane of the $CuInS_2$ tetragonal phase, equivalent to the (111) plane of the zinc-blende phase, is a polar surface, which is likely an anion- or cation-terminated surface. These polar surfaces have a higher surface energy and are very reactive. The fast growth along the [112] direction normally results in the diminishing of the (112) plane, leaving nonpolar surfaces such as (114) planes.

Surface Properties. Because of their small dimensions, NCs have an inherently large surface to volume ratio, and it has been shown in a number of systems and potential applications that surface properties play a crucial role.[7,46] As such, it is important to investigate the functionalization of the surface, determining the extent of surface coverage and the nature of the capping ligands, that tend to associate with surface atoms and surface defects. In this $CuInS_2$ system, we have introduced two surfactants in the synthetic method, allowing for the possibilities of dodecanethiol coverage, oleic acid coverage, or a presence of both ligands (dodecanethiol + oleic acid) on the surface of $CuInS_2$ nanocrystals. Figure 4a shows the Fourier transform infrared spectra (FTIR) spectra of resulting NCs in comparison with pure ligands (also see Supporting Information Figure S4). The absence of the C═O vibration mode around 1550−1700 cm^{-1} indicates that the final nanocrystalline $CuInS_2$ product contains no oleic acid on the NC surface.

Optical Properties. It has been known that the optical properties of ternary NCs depend on their size, shape, composition, and surface states.[21,35] The UV−vis absorption spectra of the as-prepared $CuInS_2$ NCs have been measured at room temperature and are shown in Figure 5a. For all samples, a broad absorption band

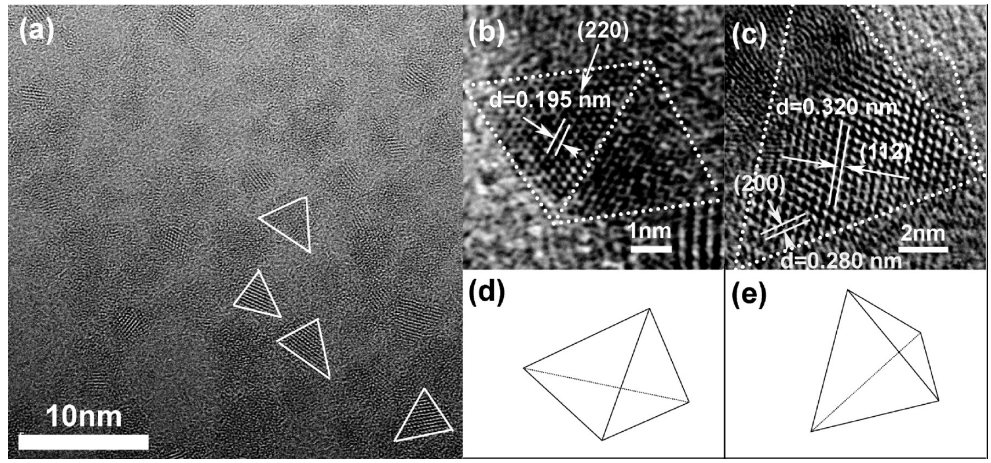

Figure 3. (a) HRTEM images of $CuInS_2$ NCs with an average diameter of 5.2 nm; (b, c) two representative HRTEM images of a single $CuInS_2$ NC; (d, e) schematic diagrams corresponding to $CuInS_2$ pyramids in b and c, respectively.

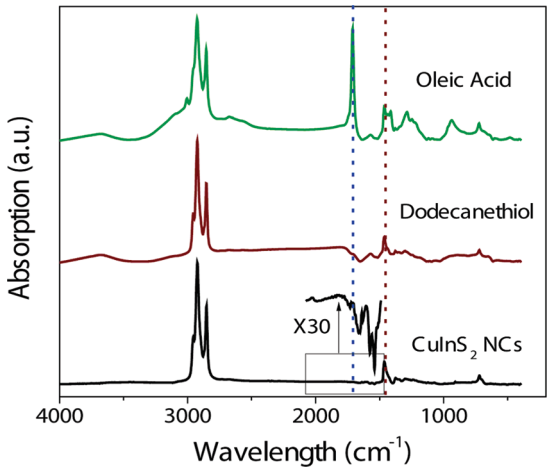

Figure 4. (a) FTIR spectrum of as synthesized $CuInS_2$ NCs in comparison to spectra of oleic acid and dodecanethiol.

is observed together with an absorption tail at longer wavelengths. As the NCs become larger, the absorption edge gradually shifts toward longer wavelengths. Similar to previous observations, no sharp absorption peak was observed for any of the samples.[21,35] The absorption coefficient of semiconductor materials is related to the density of excited states that are generated through the absorption of photons with corresponding energy. For semiconductors with direct bandgaps, it is possible to estimate the lowest excited states by the following empirical formula:[47]

$$\alpha_{h\nu} = \sqrt{(h\nu - E_x)} \qquad (2)$$

where α is the absorption coefficient, ν is the light frequency, h is Planck's constant ($h\nu$ is the energy of a photon with frequency ν), and E_x is the optical band gap energy.

Since the $CuInS_2$ nanocrystals did not possess excitonic peaks, we adapted eq 2 by plotting α^2 *versus* $h\nu$, which forms a straight line and allows us to measure the optical bandgaps of $CuInS_2$ NCs of various sizes (see Supporting Information Figure S5). Since the $CuInS_2$ NCs are nearly monodisperse, it is acceptable to measure their direct bandgap by extrapolating a straight line to the $\alpha = 0$ axis in the plots of α^2 *versus* $h\nu$. In this way, the lowest excited states, thus the optical bandgaps of $CuInS_2$ NCs were determined. The results are listed in Table 2.

TABLE 2. Comparison of the Bangaps of $CuInS_2$ NCs Determined by Absorption Spectra and Cyclic Voltammetry Measurements[a]

average sizes	3.5 nm	5.2 nm	5.6 nm	6.1 nm	7.3 nm
E_g (determined by CV) (eV)	2.04	1.88	1.80	1.78	1.70
E_x (determined by absorption) (eV)	1.945	1.798	1.757	1.719	1.668
E_b (binding energy) (meV)	~95	~82	~43	~61	~32

[a]The binding energies of $CuInS_2$ NCs with different sizes were calculated by following the equation $E_b = E_g - E_x$. Note: the exciton binding energy has at least an error bar of ~25 meV from the cyclic voltammetry measurements.

The photoluminescence (PL) spectra of $CuInS_2$ pyramids were also measured (see Supporting Information Figure S6). Similar to previous reports, the $CuInS_2$ NCs have a very broad PL emission.[21,35] It was observed that the PL emission gradually shifted to the longer wavelength in the range of NIR region (700 to ~900 nm) with the diameter increasing. Two-dimensional photoluminescence excitation (2D PLE) spectroscopy, obtained by measuring PL spectra over a range of excitation energies, contains information of PLE and PL spectra.[48] Figure 5b shows a typical 2D PLE spectrum of $CuInS_2$ pyramids. An obvious gap between excitation and emission due to the Stokes shift was observed. Compared to absorption spectra, the feature illustrating the optical band in PLE spectra is more easily identified. By drawing a vertical PLE line in the emission peak and inclined size distribution emission line along the PLE peak, we

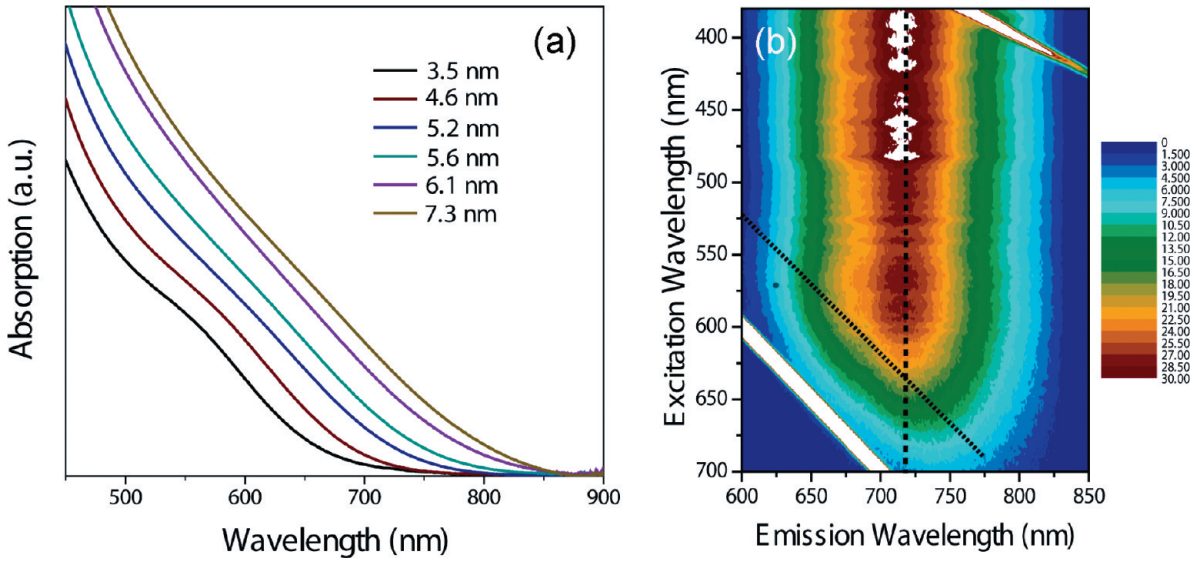

Figure 5. (a) Absorption spectra of $CuInS_2$ NCs with different average size of 3.5, 4.6, 5.3, 5.6, 6.1 and 7.3 nm; (b) 2D PLE spectra of $CuInS_2$ NCs with average diameter of 3.5 nm. The PL intensity was represented by colors.

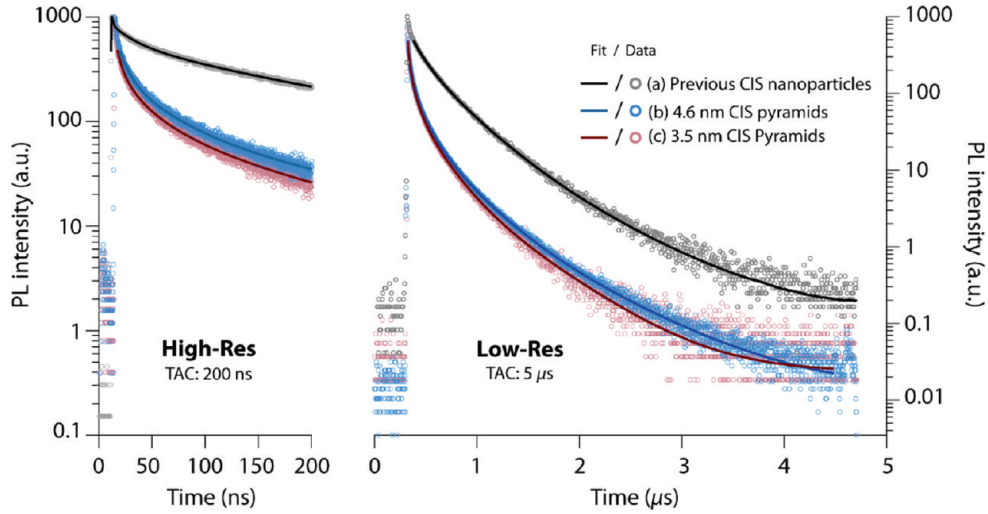

Figure 6. PL decay of $CuInS_2$ samples: (a) $CuInS_2$ nanoparticles with average diameters of 2.6 nm prepared by using previous method,[35] (b and c) $CuInS_2$ pyramids with average diameters of 4.6 and 3.5 nm.

find that the *y*-value of the intercept corresponds to the energy of the band edge exciton states, which provides the parameter of optical bandgap energies.

PL dynamics contains information about radiative and nonradiative relaxation processes. Recent research from our group has established how time-resolved PL can be used as a quantitative tool for the analysis of photoexcitation dynamics in colloidal semiconductor nanocrystals.[49,50] Long time scale decay components in the PL emission of NCs are often related to intrinsic defects and surface defects.[34−36] The time-resolved PL of a sample of NCs directly reflects the transient population that is distributed in radiative core states and indirectly indicate participation in the nonradiative relaxation process of surface-related trap states.

The time-resolved PL spectra of $CuInS_2$ NCs at their emission peak are shown in Figure 6. The PL decays are multiexponential, which likely indicates decayed PL resulting from surface traps. Such nonexponential decays are often quantified using an average PL lifetime, which is the average time, after the excitation pulse, at which an emitted photon is detected. The data was analyzed by least-squares iterative reconvolution of a model multiexponential function with an experimental instrument response function. The average lifetime was then calculated using

$$\tau_{avg} = \frac{\sum_n \alpha_n \tau_n^2}{\sum_n \alpha_n \tau_n} \qquad (3)$$

where $1/\tau_n$ is the decay constant of component n in the model multiexponential function.

It was found that the average PL lifetimes were reduced from ~300 ns for the $CuInS_2$ nanoparticles synthesized by the previous method[35] to 140−160 ns for the high quality $CuInS_2$ pyramids obtained in this work. The decrease of average PL lifetime in $CuInS_2$ pyramids can be attributed to the reduction of surface-related trap states.[49,51] Because of the high crystallinity and the faceted structure of these newly prepared $CuInS_2$ pyramids whose surface is well protected by capping ligands, it would be reasonable to conclude that the density of nonradiative surface traps is lower in these high quality $CuInS_2$ NCs.

Quantum Confinement Effects. The basic quantum confinement effects in NCs have been of great fundamental interest because it provides tunability of optical properties.[52] The quantum confinement effects in nonspherical NCs are of particular interest for their potential shape-tuning effects.[53] On the basis of the investigation of bulk film, it was determined that the chemical composition has limited influence on the optical bandgaps of $CuInS_2$ materials.[54,55] The obvious blue shift in absorption spectra should be related to quantum confinement effects. The size-dependent optical bandgap is a direct way to demonstrate the quantum confinement effects in NCs. For $CuInS_2$ NCs we plot the size-dependent optical bandgap determined from absorption and 2D PLE spectra in Figure 7. Models based on the effective mass approximation (EMA) are often used to describe the energy levels in semiconductor NCs.[56] Recently, Omata *et al.* have evaluated size dependent bandgaps of I−III−VI NCs by using the finite-depth-well EMA calculation.[57] On the basis of their calculations, the optical bandgap of I−III−VI NCs can be described by the following empirical relation:

$$x\cot(x) = 1 - \left(\frac{m^*}{m_0}\right) - \sqrt{\left(\frac{m^*}{m_0}\right)\left(\frac{V_0}{\Delta} - x^2\right)} \qquad (4)$$

where $V_0 = (E_{gcap} - E_{gbulk})/2$, $x = (\sqrt{2m^*Er_0^2/\hbar^2})^{1/2}$, E_{gcap} is the energy gap between the LUMO and the HOMO of the capping surfactant, E_{gbulk} is the energy band gap of the bulk semiconductor and r_0 is the radius of the nanoparticles. When the confinement potential is finite, there is no analytical solution of the eigenvalue equa-

tion and, hence, eq 4 is numerically solved by substituting $m^* = m^*_e$ for the electrons and $m^* = m^*_h$ for the holes. Dodecanethiol is the organic capping ligand on the $CuInS_2$ NC surface. E_{gcap} of dodecanethiol has been experimentally determined to be ~7 eV.[58] So, $E_{gcap} = 7$ eV, $m^*_e/m_0 = 0.16$, $m^*_h/m_0 = 1.3$, and $E_{gbulk} = 1.53$ eV were used for the calculation, which is represented by the black line in Figure 7. There is a very good correspondence between experimental results and the finite depth-well EMA predictions, indicating that the diameter of $CuInS_2$ NCs can be estimated by comparison of the optical bandgap with the finite-depth-well EMA calculation results.

Electrochemical Properties. Considering the application of NCs in electroluminescence and solar cell devices, the bandgaps and energy levels are vital parameters for devices design and material selections.[6,59] Cyclic voltammetry (CV) has been proven to be an effective method for the determination of bandgaps as well as the energy levels of the highest occupied molecular orbital (HOMO) and the lowest unoccupied molecular orbital (LUMO) of conjugated polymers and organic molecules.[60] This method has been successfully adapted to measure the energy levels in semiconductor NCs,[61−65] although interpretation of these data by surface states can be complicated. The oxidation process is related to the injection of a hole into the HOMO level, and the reduction process is related to the injection of an electron into the LUMO level. The energy levels (HOMO and LUMO) can be calculated from the onset oxidation potential (E^{ox}) and onset reduction potential (E^{red}), respectively, according to the following equations:

$$E_{HOMO} = -I_p = -(E^{ox} + 4.71)\ \text{eV} \quad (5)$$

$$E_{LUMO} = -E_a = -(E^{red} + 4.71)\ \text{eV} \quad (6)$$

where the unit of the potentials is V *vs* Ag/Ag^+ (0.01 M) reference electrode.

CV curves of $CuInS_2$ NCs with different average sizes deposited on a carbon electrode were measured and the results are shown in Figure 8a (a typical CV curve of a blank was shown in the Supporting Information Figure S7). According to the literature,[66] the bulk bandgap of $CuInS_2$ is 1.53 eV and their HOMO and LUMO levels are *ca.* −5.6 and −4.1 eV, respectively (these values correspond to oxidation and reduction potentials of *ca.* 0.9 and −0.6 V). Distinct peaks with potential higher than 0.9 V in the oxidation process or lower than −0.6 V in reduction processes are related to the injection of holes to the HOMO levels or electrons to the LUMO levels.[25] The onset of oxidation and reduction peaks were identified and labeled by dotted lines in Figure 8a. The corresponding bandgap values and energy levels of these samples were calculated (according to eqs 5 and 6) and shown in Table 2 and Figure 8b (see Supporting Information Table S8). The CV results can also be used

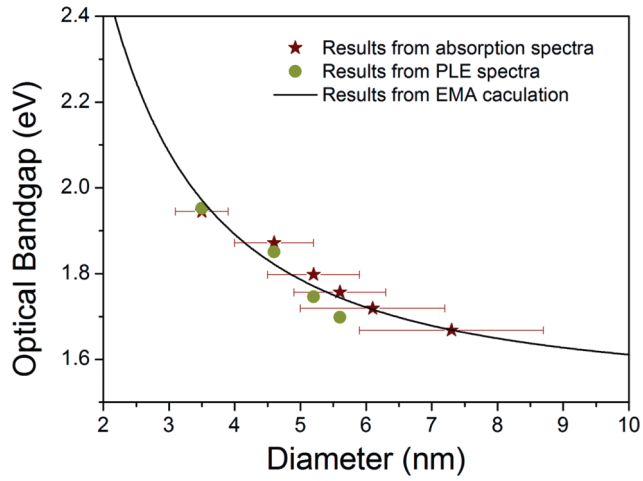

Figure 7. Size-dependent optical bandgaps of $CuInS_2$ NCs determined from absorption (red stars) and 2D PLE spectra (green spheres) illustrating quantum confinement. The solid line represents the calculation result from finite depth-well EMA theory.[57]

to estimate the size-dependent quantum confinement in $CuInS_2$ NCs. Figure 8b shows the energy levels of $CuInS_2$ NCs with different average size comparing them to bulk values. The decrease of the energy of the HOMO levels and the corresponding increase in energy of the LUMO levels are in good agreement with the theoretical expectations.

CV measurements determined the values of lowest conductive states and highest valence states, corresponding to the electronic bandgap (E_b). The spectroscopic measurements give the optical band (E_x), which corresponds to the value of the electronic bandgap (E_g) minus the exciton binding energy (E_b). Thus, the exciton binding energy (E_b) can be defined as $E_b = E_g - E_x$. We calculated the exciton binding energy by using our CV and spectroscopic experimental results. The exciton binding energy in $CuInS_2$ NCs is found to be in the range of 100−30 meV and shows a decreasing trend with increasing NC diameter, corresponding to the size-dependence of the electron−hole Coulomb interaction. This observation also provides evidence that photoexcitation of $CuInS_2$ NCs generates excitons.

CONCLUSIONS

We have further developed the noninjection method for the synthesis of monodisperse pyramidal $CuInS_2$ NCs, whose size can be tuned from 3 to 8 nm. STEM, XRD, and HRTEM characterizations show that fabricated NCs are of high quality. EDS and ICP−AES show that the resulting NCs are copper-rich for the smaller dots and become stoichiometric for the larger ones. This newly developed synthetic methodology is ideal in a number of ways as it can be easily altered to yield a high quality product on a gram scale, is highly reproducible, and is based on green chemistry. The scalability of the reaction is vital as the development of potential applications, where high quality $CuInS_2$ NCs could

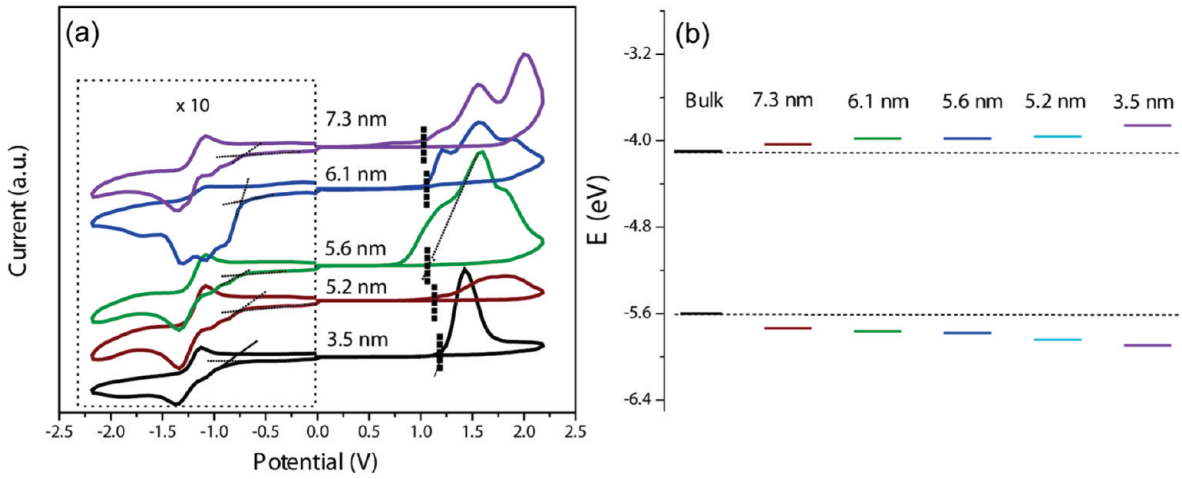

Figure 8. (a) Cyclic voltammograms of $CuInS_2$ nanocrystals with average diameters of 3.5, 5.2, 5.6, 6.1, and 7.3 nm; (b) the energy levels of $CuInS_2$ nanocrystals with different average diameters determined by cyclic voltammetry.

be integrated as light emitters and solar harvesters, would require the production of these nanomaterials at a much larger scale. To investigate the potential of the integratability of $CuInS_2$ NCs into electronic devices, we have carefully studied the surface-, optical-, and electrochemical properties of resulting NCs. The FTIR results have indicated that the surface of synthesized $CuInS_2$ NCs is functionalized with dodecanethiol capping ligands. Size-dependent bandgaps and energy levels were determined through spectroscopic and CV measurements, illustrating the presence of quantum confinement effects in this system. By comparing the bandgaps determined by CV measurements and the optical bandgaps from the spectroscopic measurements, the exciton binding energy of $CuInS_2$ pyramids was resolved. This provides evidence that the light absorbed by $CuInS_2$ NCs mainly generates photoexcited excitons. Vital parameters obtained through these experimental results can be very helpful in the design and development of high performance $CuInS_2$ NC based electronic devices. Future work will focus on the exploration of these high quality NCs for light emitting and solar harvesting applications. In addition, this method can also be simply extended to $Zn_x(CuIn)_{1-x}S_2$ and $CuGa_xIn_{1-x}S_2$ systems, which are also of interest for light emitting and solar harvesting applications.

EXPERIMENTAL SECTION

Chemicals. Copper(I) iodide (Fluka, ≥ 98%), copper(I) acetate (Strem Chemicals, 99%), indium(III) acetate (Aldrich, 99.999%), *n*-dodecanethiol (Aldrich, ≥98%), oleic acid (OA, Aldrich, 90%), and 1-octadecene (ODE, Aldrich, 90%) were used as purchased and without further purification.

Synthesis of Pyramidal $CuInS_2$ NCs. In a typical synthesis CuI (0.191 g, 1 mmol) and $In(Ac)_3$ (0.292 g, 1 mmol) were mixed with 1 mL of dodecanethiol in a 50 mL three-necked flask, which was followed by the addition of 10 mL of ODE. The mixture was then degassed at 120 °C. After 30 min, 1 mL of oleic acid was added into the reaction flask, and the solution was continuously degassed for another 30 min. After that, the solution was heated to 200 °C under argon flow and kept for a fixed time (20, 30, 45, 60, 90, 120 min). During the reaction, aliquots were taken with a syringe at different times to monitor the growth of $CuInS_2$ NCs by recording UV−vis and PL spectra (7, 20, 30, 45, 60, 90, 120 min). Afterward, the reaction solution was cooled to room temperature and precipitated by acetone. The flocculent precipitate that formed was centrifuged, while the supernatant liquid was decanted, and the isolated solid was dispersed in toluene or chloroform. The above centrifugation and isolation procedure was then repeated several times for purification of the prepared $CuInS_2$ NCs. Finally, the products were redispersed in toluene or chloroform or dried under vacuum for further analyses.

Gram-scale synthesis of the $CuInS_2$ NCs was performed by heating a mixture of 1.91 g of CuI, 2.92 g of $In(Ac)_3$, 10 mL of dodecanethiol, 10 mL of oleic acid, and 100 mL of ODE in a 500 mL three-necked flask at 200 °C for 2 h. The product yield was 80%−90% (~2.3 g of $CuInS_2$ NCs) (see Supporting Information Figure S1).

Characterizations. STEM images were acquired using a Hitachi HD-2000 instrument equipment at 200 kV. EDX spectra was performed on a Hitachi 5200 instrument equipment with an Oxford Instruments Inca EDX system operated at 20 kV. HRTEM images were recorded using a JEOL-2100F instrument equipped with a Gatan camera operated at 200 kV. XRD measurements were carried out on a Siemens D5000 diffractometer using a high-power Cu Kα source operating at 50 kV and 35 mA with a Kevex solid-state detector. A step scan mode was used for data collection with a step size of 0.028 and time of 2.0 s per step. ICP−AES measurements were performed as follows. Purified $CuInS_2$ NC samples were dried by gentle heating under argon, and then the sample was digested by 0.5 mL of aqua regia. The digested sample was transferred into a volumetric flask to make a fixed volume aqueous solution for the ICP−AES measurements. Absorption spectra and steady PL spectra were obtained on a CARY 100 BIO UV−vis spectrophotometer and CARY Varian fluorescence spectrometer, respectively. FTIR spectra in the region of 400−4000 cm^{-1} were recorded on a BRUKER TENSOR 27 with 4 cm^{-1} resolution. Photoluminescence decays were measured by time-resolved single photon counting using an IBH Datastation Hub system coupled to an IBH 5000 M monochromator and a R3809U-50 cooled MCP PMT detector. The samples were excited at 450 nm using a Ti:sapphire Tsunami laser model 3950 ps with a GWU-23PL multiharmonic generator, both from Spectra-Physics. Cyclic voltammograms (CVs) were recorded on a Zahner IM6e electrochemical workstation, using glassy carbon discs as the working electrode (~ 0.25 cm^2), a Pt wire as the counter-electrode, and Ag/Ag^+ (Ag wires with 0.01 M $AgNO_3$ in acetonitrile) as the reference electrode; 0.1 M tetrabutylammoniumhexafluorophosphate ($TBAPF_6$) dissolved in acetonitrile was

employed as the supporting electrolyte. All NC samples were purified and redissolved in chloroform. The working electrodes were polished, cleaned, and dried before depositing the NC samples. A drop of diluted NC solution was deposited onto the surface of the working electrode to form a NC film. The scan rate was set at 50 mV/s, and during all the experiments, the electrolyte solutions were thoroughly deoxygenated by bubbling high purity nitrogen for 15 min. A nitrogen atmosphere was maintained over the solution.

Acknowledgment. The Natural Sciences and Engineering Research Council of Canada is gratefully acknowledged for support of this research. The authors thank N. Coombs, S. Petrov, B. Chen, F. Jiang, and Y. Zhao for assistance with material characterizations and Y. Zhang and J. Tang for valuable discussions and help.

Supporting Information Available: The high magnification STEM images, illustration of diameter determination, illustration of shape treatment of Scherrer equation, plots of absorption coefficient and photon energy, additional FTIR spectra, CV blank and parameters of CV results. This material is available free of charge *via* the Internet at http://pubs.acs.org.

REFERENCES AND NOTES

1. Scholes, G. D. Controlling the Optical Properties of Inorganic Nanoparticles. *Adv. Funct. Mater.* **2008**, *18*, 1157–1172.
2. Talapin, D. V.; Lee, J. S.; Kovalenko, M. V.; Shevchenko, E. V. Prospects of Colloidal Nanocrystals for Electronic and Optoelectronic Applications. *Chem. Rev.* **2010**, *110*, 389–458.
3. Kamat, P. V. Quantum Dot Solar Cells. Semiconductor Nanocrystals as Light Harvesters. *J. Phys. Chem. C* **2008**, *112*, 18737–18753.
4. Bruchez, M.; Moronne, M.; Gin, P.; Weiss, S.; Alivisatos, A. P. Semiconductor Nanocrystals as Fluorescent Biological Labels. *Science* **1998**, *281*, 2013–2016.
5. Klimov, V. I.; Ivanov, S. A.; Nanda, J.; Achermann, M.; Bezel, I.; McGuire, J. A.; Piryatinski, A. Single-Exciton Optical Gain in Semiconductor Nanocrystals. *Nature* **2007**, *447*, 441–446.
6. Sun, Q.; Wang, Y. A.; Li, L. S.; Wang, D. Y.; Zhu, T.; Xu, J.; Yang, C. H.; Li, Y. F. Bright, Multicoloured Light-Emitting Diodes Based on Quantum Dots. *Nat. Photon.* **2007**, *1*, 717–722.
7. Huynh, W. U.; Dittmer, J. J.; Alivisatos, A. P. Hybrid Nanorod-Polymer Solar Cells. *Science* **2002**, *295*, 2425–2427.
8. Hines, M. A.; Scholes, G. D. Colloidal PbS Nanocrystals with Size-Tunable Near-Infrared Emission: Observation of Post-Synthesis Self-Narrowing of the Particle Size Distribution. *Adv. Mater.* **2003**, *15*, 1844–1849.
9. Sargent, E. H. Infrared Photovoltaics Made by Solution Processing. *Nat. Photon.* **2009**, *3*, 325–331.
10. Nakamura, H.; Kato, W.; Uehara, M.; Nose, K.; Omata, T.; Otsuka-Yao-Matsuo, S.; Miyazaki, M.; Maeda, H. Tunable Photoluminescence Wavelength of Chalcopyrite $CuInS_2$-Based Semiconductor Nanocrystals Synthesized in a Colloidal System. *Chem. Mater.* **2006**, *18*, 3330–3335.
11. Zhong, H. Z.; Li, Y. C.; Ye, M. F.; Zhu, Z. Z.; Zhou, Y.; Yang, C. H.; Li, Y. F. A Facile Route to Synthesize Chalcopyrite $CuInSe_2$ Nanocrystals in Non-coordinating Solvent. *Nanotechnology* **2007**, *18*, 025602.
12. Allen, P. M.; Bawendi, M. G. Ternary I−III−VI Quantum Dots Luminescent in the Red to Near-Infrared. *J. Am. Chem. Soc.* **2008**, *130*, 9240–9241.
13. Guo, Q.; Kim, S. J.; Kar, M.; Shafarman, W. N.; Birkmire, R. W.; Stach, E. A.; Agrawal, R.; Hillhouse, H. W. Development of $CuInSe_2$ Nanocrystal and Nanoring Inks for Low-Cost Solar Cells. *Nano Lett.* **2008**, *8*, 2982–2987.
14. Tang, J.; Hinds, S.; Kelley, S. O.; Sargent, E. H. Synthesis of Colloidal $CuGaSe_2$, $CuInSe_2$, and $Cu(InGa)Se_2$ Nanoparticles. *Chem. Mater.* **2008**, *20*, 6906–6910.
15. Panthani, M. G.; Akhavan, V.; Goodfellow, B.; Schmidtke, J. P.; Dunn, L.; Dodabalapur, A.; Barbara, P. F.; Korgel, B. A. Synthesis of $CuInS_2$, $CuInSe_2$, and $Cu(In_xGa_{1-x})Se_2$ (CIGS) Nanocrystal "Inks" for Printable Photovoltaics. *J. Am. Chem. Soc.* **2008**, *130*, 16770–16777.
16. Kuo, K. T.; Liu, D. M.; Chen, S. Y.; Lin, C. C. Core−Shell $CuInS_2$/ZnS Quantum Dots Assembled on Short ZnO Nanowires with Enhanced Photo-conversion Efficiency. *J. Mater. Chem.* **2009**, *19*, 6780–6788.
17. Guo, Q.; Ford, G. M.; Hillhouse, H. W.; Agrawal, R. Sulfide Nanocrystal Inks for Dense $Cu(In_{1-x}Ga_x)(S_{1-y}Se_y)_2$ Absorber Films and Their Photovoltaic Performance. *Nano Lett.* **2009**, *9*, 3060–3065.
18. Li, L.; Coates, N.; Moses, D. Solution-Processed Inorganic Solar Cell Based on *in Situ* Synthesis and Film Deposition of $CuInS_2$ Nanocrystals. *J. Am. Chem. Soc.* **2010**, *132*, 22–23.
19. Weil, B. D.; Connor, S. T.; Cui, Y. $CuInS_2$ Solar Cells by Air-Stable Ink Rolling. *J. Am. Chem. Soc.* **2010**, *132*, 6642–6643.
20. Li, T. L.; Teng, H. S. Solution Synthesis of High-Quality $CuInS_2$ Quantum Dots as Sensitizers for TiO_2 Photoelectrodes. *J. Mater. Chem.* **2010**, *20*, 3656–3664.
21. Xie, R. G.; Rutherford, M.; Peng, X. G. Formation of High-Quality I−III−VI Semiconductor Nanocrystals by Tuning Relative Reactivity of Cationic Precursors. *J. Am. Chem. Soc.* **2009**, *131*, 5691–5697.
22. Batabyal, S. K.; Tian, L.; Venkatram, N.; Ji, W.; Vittal, J. J. Phase-Selective Synthesis of $CuInS_2$ Nanocrystals. *J. Phys. Chem. C* **2009**, *113*, 15037–15042.
23. Nose, K.; Soma, Y.; Omata, T.; Otsuka-Yao-Matsuo, S. Synthesis of Ternary $CuInS_2$ Nanocrystals; Phase Determination by Complex Ligand Species. *Chem. Mater.* **2009**, *21*, 2607–2613.
24. Koo, B.; Patel, R. N.; Korgel, B. A. Wurtzite−Chalcopyrite Polytypism in $CuInS_2$ Nanodisks. *Chem. Mater.* **2009**, *21*, 1962–1966.
25. Norako, M. E.; Franzman, M. A.; Brutchey, R. L. Growth Kinetics of Monodisperse Cu−In−S Nanocrystals Using a Dialkyl Disulfide Sulfur Source. *Chem. Mater.* **2009**, *21*, 4299–4304.
26. Du, W. M.; Qian, X. F.; Yin, J.; Gong, Q. Shape- and Phase-Controlled Synthesis of Monodisperse, Single-Crystalline Ternary Chalcogenide Colloids through a Convenient Solution Synthesis Strategy. *Chem.—Eur. J.* **2007**, *13*, 8840–8846.
27. Wang, D. S.; Zheng, W.; Hao, C. H.; Peng, Q.; Li, Y. D. General Synthesis of I−III−VI_2 Ternary Semiconductor Nanocrystals. *Chem. Commun.* **2008**, 2556–2558.
28. Connor, S. T.; Hsu, C. M.; Weil, B. D.; Aloni, S.; Cui, Y. Phase Transformation of Biphasic Cu_2S−$CuInS_2$ to Monophasic $CuInS_2$ Nanorods. *J. Am. Chem. Soc.* **2009**, *131*, 4962–4966.
29. Castro, S. L.; Bailey, S. G.; Raffaelle, R. P.; Banger, K. K.; Hepp, A. F. Nanocrystalline Chalcopyrite Materials ($CuInS_2$ and $CuInSe_2$) *via* Low-Temperature Pyrolysis of Molecular Single-Source Precursors. *Chem. Mater.* **2003**, *15*, 3142–3147.
30. Castro, S. L.; Bailey, S. G.; Raffaelle, R. P.; Banger, K. K.; Hepp, A. F. Synthesis and Characterization of Colloidal $CuInS_2$ Nanoparticles from a Molecular Single-Source Precursor. *J. Phys. Chem. B* **2004**, *108*, 12429–12435.
31. Pan, D. C.; An, L. J.; Sun, Z. M.; Hou, W.; Yang, Y.; Yang, Z. Z.; Lu, Y. F. Synthesis of Cu−In−S Ternary Nanocrystals with Tunable Structure and Composition. *J. Am. Chem. Soc.* **2008**, *130*, 5620–5621.
32. Dutta, D. P.; Sharma, G.; Tyagi, A. K. A Facile Synthesis of $CuInS_2$ Nanoparticles from Molecular Single Source Precursors. *J. Nanosci. Nanotechnol.* **2007**, *7*, 4353–4358.
33. Gardner, J. S.; Shurdha, E.; Wang, C. M.; Lau, L. D.; Rodriguez, R. G.; Pak, J. J. Rapid Synthesis and Size Control of $CuInS_2$ Semiconductor Nanoparticles Using Microwave Irradiation. *J. Nanopart. Res.* **2008**, *10*, 633–641.
34. Uehara, M.; Watanabe, K.; Tajiri, Y.; Nakamura, H.; Maeda, H. Synthesis of $CuInS_2$ Fluorescent Nanocrystals and Enhancement of Fluorescence by Controlling Crystal Defect. *J. Chem. Phys.* **2008**, *129*, 234709.
35. Zhong, H. Z.; Zhou, Y.; Ye, M. F.; He, Y. J.; Ye, J. P.; He, C.;

Yang, C. H.; Li, Y. F. Controlled Synthesis and Optical Properties of Colloidal Ternary Chalcogenide $CuInS_2$ Nanocrystals. *Chem. Mater.* **2008**, *20*, 6434–6443.
36. Li, L.; Daou, T. J.; Texier, I.; Tran, T. K. C.; Nguyen, Q. L.; Reiss, P. Highly Luminescent $CuInS_2$/ZnS Core/Shell Nanocrystals: Cadmium-free Quantum Dots for *in Vivo* Imaging. *Chem. Mater.* **2009**, *21*, 2422–2429.
37. Pearson, R. G. Hard and Soft Acids and Bases. *J. Am. Chem. Soc.* **1963**, *85*, 3533–3539.
38. Yang, Y. A.; Wu, H. M.; Williams, K. R.; Cao, Y. C. Synthesis of CdSe and CdTe Nanocrystals without Precursor Injection. *Angew. Chem., Int. Ed.* **2005**, *44*, 6712–6715.
39. Langford, J. I.; Wilson, A. J. C. Scherrer after 60 Years—Survey and Some New Results in Determination of Crystallite Size. *J. Appl. Crystallogr.* **1978**, *11*, 102–113.
40. Natter, H.; Schmelzer, M.; Loffler, M. S.; Krill, C. E.; Fitch, A.; Hempelmann, R. Grain-Growth Kinetics of Nanocrystalline Iron Studied *in Situ* by Synchrotron Real-Time X-ray Diffraction. *J. Phys. Chem. B* **2000**, *104*, 2467–2476.
41. Nanda, J.; Sapra, S.; Sarma, D. D.; Chandrasekharan, N.; Hodes, G. Size-Selected Zinc Sulfide Nanocrystallites: Synthesis, Structure, and Optical Studies. *Chem. Mater.* **2000**, *12*, 1018–1024.
42. Borchert, H.; Shevehenko, E. V.; Robert, A.; Mekis, I.; Kornowski, A.; Grubel, G.; Weller, H. Determination of Nanocrystal Sizes: A Comparison of TEM, SAXS, and XRD Studies of Highly Monodisperse $CoPt_3$ Particles. *Langmuir* **2005**, *21*, 1931–1936.
43. Greyson, E. C.; Barton, J. E.; Odom, T. W. Tetrahedral Zinc Blende Tin Sulfide Nano-and Microcrystals. *Small* **2006**, *2*, 368–371.
44. Manna, L.; Milliron, D. J.; Meisel, A.; Scher, E. C.; Alivisatos, A. P. Controlled Growth of Tetrapod-Branched Inorganic Nanocrystals. *Nat. Mater.* **2003**, *2*, 382–385.
45. Koo, B.; Patel, R. N.; Korgel, B. A. Synthesis of $CuInSe_2$ Nanocrystals with Trigonal Pyramidal Shape. *J. Am. Chem. Soc.* **2009**, *131*, 3134–3135.
46. Tang, J.; Brzozowski, L.; Barkhouse, D. A. R.; Wang, X. H.; Debnath, R.; Wolowiec, R.; Palmiano, E.; Levina, L.; Pattantyus-Abraham, A. G.; Jamakosmanovic, D.; *et al.* Quantum Dot Photovoltaics in the Extreme Quantum Confinement Regime: The Surface-Chemical Origins of Exceptional Air- and Light-Stability. *ACS Nano* **2010**, *4*, 869–878.
47. Huxter, V. M.; Mirkovic, T.; Nair, P. S.; Scholes, G. D. Demonstration of Bulk Semiconductor Optical Properties in Processable Ag_2S and EuS Nanocrystalline Systems. *Adv. Mater.* **2008**, *20*, 2439–2443.
48. Zhong, H.; Nagy, M.; Jones, M.; Scholes, G. D. Electronic States and Exciton Fine Structure in Colloidal CdTe Nanocrystals. *J. Phys. Chem. C* **2009**, *113*, 10465–10470.
49. Jones, M.; Lo, S. S.; Scholes, G. D. Quantitative Modeling of the Role of Surface Traps in CdSe/CdS/ZnS Nanocrystal Photoluminescence Decay Dynamics. *Proc. Natl. Acad. Sci. U.S.A.* **2009**, *106*, 3011–3016.
50. Jones, M.; Scholes, G. D. On the Use of Time-Resolved Photoluminescence as a Probe of Nanocrystal Photoexcitation Dynamics. *J. Mater. Chem.* **2010**, *20*, 3533–3538.
51. Zhong, H. Z.; Lo, S. S.; Scholes G. D. Unpublished results.
52. Scholes, G. D.; Rumbles, G. Excitons in Nanoscale Systems. *Nat. Mater.* **2006**, *5*, 683–696.
53. Kim, J.; Nair, P. S.; Wong, C. Y.; Scholes, G. D. Sizing Up the Exciton in Complex-Shaped Semiconductor Nanocrystals. *Nano Lett.* **2007**, *7*, 3884–3890.
54. Shi, Y.; Jin, Z. G.; Li, C. Y.; An, H. S.; Qiu, J. J. Effect of [Cu]/[In] Ratio on Properties of $CuInS_2$ Thin Films Prepared by Successive Ionic Layer Absorption and Reaction Method. *Appl. Surf. Sci.* **2006**, *252*, 3737–3743.
55. Guillen, C.; Herrero, J. $CuInS_2$ and $CuGaS_2$ Thin Films Grown by Modulated Flux Deposition with Various Cu Contents. *Phys. Status Solidi* **2006**, *203*, 2438–2443.
56. Brus, L. E. Electron−Electron and Electron−Hole Interactions in Small Semiconductor Crystallites: The Size Dependence of the Lowest Excited Electronic State. *J. Appl. Phys.* **1984**, *80*, 4403.
57. Omata, T.; Nose, K.; Otsuka-Yao-Matsuo, S. Size Dependent Optical Band Gap of Ternary I−III−VI2 Semiconductor Nanocrystals. *J. Appl. Phys.* **2009**, *105*, 073106.
58. Salomon, A.; Cahen, D.; Lindsay, S.; Tomfohr, J.; Engelkes, V. B.; Frisbie, C. D. Comparison of Electronic Transport Measurements on Organic Molecules. *Adv. Mater.* **2003**, *15*, 1881–1890.
59. Zhou, Y.; Li, Y. C.; Zhong, H. Z.; Hou, J. H.; Ding, Y. Q.; Yang, C. H.; Li, Y. F. Hybrid Nanocrystal/Polymer Solar Cells Based on Tetrapod-Shaped $CdSe_xTe_{1-x}$ Nanocrystals. *Nanotechnology* **2006**, *17*, 4041–4047.
60. Sun, Q. J.; Wang, H. Q.; Yang, C. H.; Li, Y. F. Synthesis and Electroluminescence of Novel Copolymers Containing Crown Ether Spacers. *J. Mater. Chem.* **2003**, *13*, 800–806.
61. Bard, A. J.; Ding, Z. F.; Myung, N., Electrochemistry and Electrogenerated Chemiluminescence of Semiconductor Nanocrystals in Solutions and in Films. *Structure and Bonding: Semiconductor Nanocrystals and Silicate Naoparticles*; Mingos, D. M. P. Ed.; Springer: Berlin, 2005; Vol. 118, pp 1−57.
62. Kucur, E.; Riegler, J.; Urban, G. A.; Nann, T. Determination of Quantum Confinement in CdSe Nanocrystals by Cyclic Voltammetry. *J. Chem. Phys.* **2003**, *119*, 2333–2337.
63. Yu, D.; Wang, C. J.; Guyot-Sionnest, P. n-Type Conducting CdSe Nanocrystal Solids. *Science* **2003**, *300*, 1277–1280.
64. Poznyak, S. K.; Osipovich, N. P.; Shavel, A.; Talapin, D. V.; Gao, M. Y.; Eychmuller, A.; Gaponik, N. Size-Dependent Electrochemical Behavior of Thiol-Capped CdTe Nanocrystals in Aqueous Solution. *J. Phys. Chem. B* **2005**, *109*, 1094–1100.
65. Li, Y. C.; Zhong, H. Z.; Li, R.; Zhou, Y.; Yang, C. H.; Li, Y. F. High-Yield Fabrication and Electrochemical Characterization of Tetrapodal CdSe, CdTe, and $CdSe_xTe_{1-x}$ Nnanocrystals. *Adv. Funct. Mater.* **2006**, *16*, 1705–1716.
66. Arici, E.; Sariciftci, N. S.; Meissner, D. Hybrid Solar Cells Based on Nanoparticles of $CuInS_2$ in Organic Matrices. *Adv. Funct. Mater.* **2003**, *13*, 165–171.